

Measurement of ω and ϕ meson production via
dimuons at forward rapidity in pp collisions at
 $\sqrt{s} = 13.6$ TeV with ALICE.

Masahiro Oida

Contents

1	Introduction	1
1.1	QCD	1
1.2	Chiral symmetry	2
1.3	NJL model	3
1.4	Quark-Gluon Plasma (QGP)	5
1.5	Heavy Ion collision	6
1.6	Dilepton Measurement[5]	7
1.7	Search for chiral symmetry restoration in QGP	9
1.8	Analysis of pp collision data as a baseline	10
2	Detector setup	11
2.1	Large Hadron Collider (LHC)	11
2.2	A Large Ion Collider Experiment (ALICE)	11
2.2.1	MUON Spectrometer	12
2.2.2	MFT	13
2.2.3	MFT-MUON Track Matching	13
3	Analysis	14
3.1	DataSet	14
3.2	Event selection	14
3.3	Single muon track reconstruction	14
3.4	Single muon selection	15
3.5	Dimuon analysis	15
3.5.1	Dimuon reconstruction	15
3.5.2	Combinatorial background subtraction	16
3.5.3	Peak extraction of $\omega \rightarrow \mu\mu, \phi \rightarrow \mu\mu$	19
3.5.4	Yield calculation of ω, ϕ	20
3.6	Analysis for improving MFT-MCH matching purity	21
3.6.1	MFT-MCH matching χ^2 Optimization	21
3.7	Fake Match Track Removal Analysis of MFT-MCH-MID Track using MFT Track η - MCH Track η	24
4	Results and Outlook	28
5	Acknowledgements	28

Abstract

The masses of hadrons are theoretically explained to dynamically get their mass through the spontaneous chiral symmetry breaking. Hadrons are composed of quarks and gluons. Quarks and gluons obey quantum chromodynamics (QCD), which leads to confinement phenomena and spontaneous chiral symmetry breaking. Then, when the quarks and gluons reaches an ultra-high temperature and dense state, they undergoes a phase transition from the hadron to the quark-gluon plasma(QGP) state. In the QGP state, quarks deconfinement and it suggest the chiral symmetry restoration. The existence of the QGP has been confirmed by heavy-ion collision. Chiral symmetry restoration phenomenon has been explored via dilepton measurement. However, its phenomena have not yet been clearly unreveal, as they can also be explained by other phenomena such as the broadening of ρ mesons due to high-temperature hadron gas.

Therefore, I aim to explore chiral symmetry restoration via dimuon using ALICE in LHC Run3, and by revealing the transverse momentum dependence of the light vector mesons invariant mass distribution change in PbPb collisions. The Large Hadron Collider(LHC) is the world's largest hadron collider. The ALICE experiment has detectors specialized to QGP research, and high muon particle identification detectors in the forward region. The light vector mesons (ρ, ω, ϕ) are probes of hadron's masses inside QGP due to decay into only dimuons and have short lifetime. The advantage of using muons is that they don't include π^0 Dalitz decays and γ conversion. Therefore it is a better S/N than dielectron measurement. Furthermore, a new silicon detector (MFT) has been installed to the forward region from LHC Run3. It enables accurate measurement of the muon production point and lower transverse momentum than Run2. As a result, it enables removal of muons from heavy flavor using lifetime differences. Also the accuracy of the pseudorapidity and azimuth angle measurement of muons improves the mass resolution.

This thesis shows the transverse momentum dependence of ω and ϕ mesons invariant mass using forward dimuons in $\sqrt{s} = 13.6$ TeV pp collisions with ALICE, as a step toward measuring the modified in the invariant mass distribution of light vector mesons induced by QGP. The dimuon invariant mass was calculated using track reconstruction with forward region detectors, including MFT. A fit was performed on the ω and ϕ peak extracted from it and the yield was calculated. Along with this analysis, the matching χ^2 between the MFT and its backward detector, the MCH track, was optimised. Concerning the matching of MFT and MCH tracks, a removal analysis of incorrectly matched tracks was also carried out. It is shown that a cut applied to the pseudorapidity difference between MFT and MCH tracks, formed using all forward detectors, can remove incorrectly matched tracks.

1 Introduction

1.1 QCD

The fundamental components of the matter around us are elementary particles. The behaviour of elementary particles, such as quarks and gluons, is described by quantum field theory. In particular, quarks and gluons possess degrees of freedom called "color," the physics governing this degree of freedom is known as Quantum Chromodynamics (QCD). QCD is based on an SU(3) gauge theory and describes the strong interaction. The QCD Lagrangian is expressed as follows:

$$\mathcal{L}_{QCD} = \sum_q \bar{\psi}_{q,a} (i\gamma^\mu \partial_\mu - m_q) \psi_{q,a} + g_s \sum_q \bar{\psi}_{q,a} \gamma^\mu T^A_{ab} \psi_{q,b} G_\mu^A - \frac{1}{4} G_{\mu\nu}^A G^{A\mu\nu} \quad (1)$$

$\psi_{q,a}$ and $\bar{\psi}^* q, a$ represent the quark and antiquark fields, where q denotes the flavor degree of freedom, and a denotes the color degree of freedom. γ^μ is the gamma matrices, m_q is the particle mass corresponding to each flavor, g_s is the QCD coupling constant, $T^A * ab$ are the generator matrices, G_μ^A is the gluon field, and $G_{\mu\nu}^A$ is the gluon field tensor.

The first term in (1) represents the term for a free particle of mass m , the second term represents the interaction between quarks and gluons, and the third term represents the interaction between gluons themselves. A significant difference from Quantum Electrodynamics (QED), which describes electromagnetic interactions, is the presence of the coupling constant $\alpha_s(Q^2)$ and the self-interaction of the gluon field. In QED, the coupling constant does not depend on the energy scale. However, the coupling constant $\alpha_s(Q^2)$ that appears in QCD depends on the energy scale. Figure 1 shows how the coupling

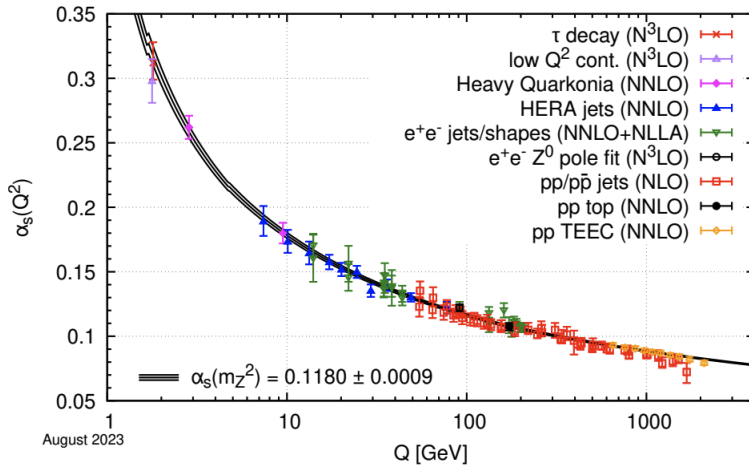


Figure 1: QCD coupling constant[1]

constant $\alpha_s(Q^2)$ changes with the energy scale. The coupling constant becomes small at high energy scales, corresponding to short distances. This reflects the phenomenon of asymptotic freedom, where quarks behave as free particles when they are sufficiently close

to each other. On the other hand, at low energy scales corresponding to long distances, the coupling constant grows infinitely large. This represents the phenomenon of quark confinement, where quarks cannot be isolated as individual particles.

Next, I describe the self-interaction of gluons. The gluon field tensor is expressed as:

$$G_{\mu\nu}^A = \partial_\mu G_\nu^A - \partial_\nu G_\mu^A + g_s f^{ABC} G_\mu^B G_\nu^C \quad (2)$$

where f^{ABC} are the structure constants of the SU(3) group. Substituting this into the third term of (1), we obtain:

$$\begin{aligned} -\frac{1}{4}G_{\mu\nu}^A G^{A\mu\nu} &= -\frac{1}{4}(\partial_\mu G_\nu^A - \partial_\nu G_\mu^A + g_s f^{ABC} G_\mu^B G_\nu^C)(\partial^\mu G^{A\nu} - \partial^\nu G^{A\mu} + g_s f^{ABC} G^{B\mu} G^{C\nu}) \\ &= -\frac{1}{4}(\partial_\mu G_\nu^A - \partial_\nu G_\mu^A)(\partial^\mu G^{A\nu} - \partial^\nu G^{A\mu}) \\ &\quad - g_s f^{ABC} G_\mu^B G_\nu^C \partial^\mu G^{A\nu} - g_s^2 f^{ABE} f^{CDE} G_\mu^A G_\nu^B G^{C\mu} G^{D\nu} \end{aligned} \quad (3)$$

In (3), the first term represents the free gluon field without interactions. The second term represents interactions involving three gluon fields, representing reactions such as $g + g \rightarrow g$. The third term corresponds to interactions involving four gluon fields, representing reactions such as $g + g \rightarrow g + g$. For photons, the third term in (2) does not exist, so the second and third terms in (3) do not appear. This is because gluons interact with each other due to their color degrees of freedom, which gives rise to gluon self-interaction.

These characteristics—namely, the energy dependence of the coupling constant and the self-interaction of gluons—contribute to the complex structure of the quark-gluon interactions.

1.2 Chiral symmetry

The quark field can be separated into its right-handed and left-handed components. The projection operators for the right-handed and left-handed components are defined as P_R and P_L , respectively. Using the γ matrices, they are expressed as follows:

$$P_R = \frac{1 + \gamma_5}{2}, \quad P_L = \frac{1 - \gamma_5}{2} \quad (4)$$

The following equations hold for these projection operators.

$$P_R + P_L = 1, \quad P_R P_L = 0, \quad P_R^2 = P_R, \quad P_L^2 = P_L \quad (5)$$

The right-handed quark field q_R and the left-handed quark field q_L are expressed using the projection operators as follows:

$$q_R = P_R q, \quad q_L = P_L q \quad (6)$$

These components are applied to the QCD Lagrangian:

$$\mathcal{L}_{QCD} = \sum_q \bar{q}(i\gamma^\mu D_\mu - m)q \quad (7)$$

- Kinetic Term (First Term of the QCD Lagrangian)

$$\bar{q}(i\gamma^\mu D_\mu)q = \bar{q}(i\gamma^\mu D_\mu)(P_R^2 + P_L^2)q \quad (8)$$

$$= \bar{q}P_L(i\gamma^\mu D_\mu)P_Rq + \bar{q}P_R(i\gamma^\mu D_\mu)P_Lq \quad (9)$$

$$= \bar{q}_R(i\gamma^\mu D_\mu)q_R + \bar{q}_L(i\gamma^\mu D_\mu)q_L \quad (10)$$

- Mass Term (Second Term of the QCD Lagrangian)

$$\bar{q}mq = \bar{q}m(P_R^2 + P_L^2)q \quad (11)$$

$$= \bar{q}P_R m P_R q + \bar{q}P_L m P_L q \quad (12)$$

$$= \bar{q}_L m q_R + \bar{q}_R m q_L \quad (13)$$

From the above, the kinetic term of the quark field can be separated into the right-handed and left-handed quark fields, thereby preserving chiral symmetry. However, the mass term mixes the right-handed and left-handed quark fields, breaking chiral symmetry. Considering the chiral limit ($m_q = 0$), the QCD Lagrangian preserves chiral symmetry.

The order parameter for the spontaneous breaking of chiral symmetry is represented by the quark condensate $\langle \bar{q}q \rangle$. As shown in Figure 2, this quantity takes a finite value in the ground state of hadrons at standard temperature and density. But, it is expected to approach $\langle \bar{q}q \rangle \sim 0$ at extremely high temperatures and densities.

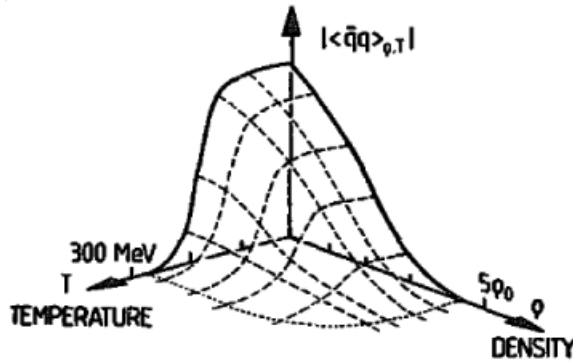


Figure 2: Quark condensate[2]

Since the vacuum expectation value of the quark condensate cannot be directly measured, as described later, various other probes are used to investigate the restoration of chiral symmetry.

1.3 NJL model

The interaction between quarks and gluons, as described in 1.1, exhibits a complex structure, making it difficult to understand various phenomena from first-principle calculations. Therefore, models are employed to describe various phenomena. One such model is the

Nambu-Jona-Lasinio (NJL) model, a chiral effective model. Its Lagrangian is expressed as follows:

$$\mathcal{L} = \bar{q}i\gamma \cdot \partial q - (-g)[(\bar{q}q)^2 + (\bar{q}i\gamma_5 q)^2] \quad (14)$$

where, q and \bar{q} represent quark and antiquark fields, respectively; γ and γ_5 are gamma matrices, with $\gamma_5 = i\gamma_0\gamma_1\gamma_2\gamma_3$. Since there is an attractive force between quarks and antiquarks, the coupling constant g is positive and has a dimension of [mass] $^{-2}$. This model serves as a chiral effective theory for QCD at the energy scale of 1 GeV. To determine the ground state of this Lagrangian, the self-consistent mean field approximation (MFA) is employed:

$$\langle \bar{q}q \rangle \equiv \frac{-m_0^2\sigma}{G} \quad (15)$$

$$\langle \bar{q}i\gamma_5 q \rangle \equiv \frac{-m_0^2\pi}{G} \quad (16)$$

By substituting (15) and (16) into (14), the expression is reformulated. Defining $\sigma = \bar{q}q$, $\pi = \bar{q}i\gamma_5 q$, and $2g = (G/m_0)^2$, we get:

$$\mathcal{L}_{MFA} = \bar{q}[i\gamma \cdot \partial - G(\sigma + i\pi\gamma_5)]q - \frac{m_0^2}{2}(\sigma^2 + \pi^2) \quad (17)$$

where, defining $q_\theta = e^{i\gamma_5 \frac{\theta}{2}}q$, $G\sqrt{\sigma^2 + \pi^2} = M$, and $\pi/\sigma = \tan\theta$, the Hamiltonian can be expressed as follows. θ is the parameter of the chiral transformation.

$$H_{MFA} = \int d^3x \left\{ \bar{q}_\theta(x)(-i\gamma \cdot \nabla + M)q_\theta(x) + \frac{m_0^2}{2}\sigma_0^2 \right\} \quad (18)$$

where $\sigma_0^2 = \sigma^2 + \pi^2$. Since π is considered sufficiently small, we write σ to σ_0 . From this Hamiltonian, the Dirac equation for mass M can be derived. Its solution is given as:

$$q_\theta(x) = \frac{1}{\sqrt{V}} \sum_{\mathbf{p}, r=\pm} \sqrt{\frac{M}{E_p}} \left\{ a_M(\mathbf{p}, r)u_M(\mathbf{p}, r)e^{-i\mathbf{p}\cdot x} + b_M^\dagger(\mathbf{p}, r)v_M(\mathbf{p}, r)e^{i\mathbf{p}\cdot x} \right\} \quad (19)$$

where, r represents helicity, $E_p = \sqrt{\mathbf{p}^2 + M^2}$, and $M = -g \langle \bar{q}_\theta q_\theta \rangle$. Next, when $q_\theta(x)$ is expanded using spinors with zero mass, the solution is:

$$q_\theta(x) = \frac{1}{\sqrt{V}} \sum_{\mathbf{p}, s=R,L} \left\{ a_{\mathbf{p}}^{(s)}(t)u_0(\mathbf{p}, s)e^{-i\mathbf{p}\cdot x} + b_{\mathbf{p}}^{(s)\dagger}(t)v_0(\mathbf{p}, s)e^{i\mathbf{p}\cdot x} \right\} \quad (20)$$

where s represents helicity. Using the solutions (19) and (20), the Hamiltonian (18) can be expressed in terms of operators for massive and massless states. Here, $a_{\mathbf{p}}$ and $b_{\mathbf{p}}$ are expansion coefficients:

$$\begin{aligned} H_{MFA} &= \sum_{\mathbf{p}, s} \left\{ |\mathbf{p}| \left(a_{\mathbf{p}}^{(s)\dagger}(t)a_{\mathbf{p}}^{(s)}(t) - b_{-\mathbf{p}}^{(s)}(t)b_{-\mathbf{p}}^{(s)\dagger}(t) \right) \right\} \\ &\quad + M \left(b_{-\mathbf{p}}^{(s)}(t)a_{\mathbf{p}}^{(s)}(t) + a_{\mathbf{p}}^{(s)\dagger}(t)b_{-\mathbf{p}}^{(s)\dagger}(t) \right) + V \frac{m_0^2}{2}\sigma_0^2 \end{aligned} \quad (21)$$

$$= \sum_{\mathbf{p}, r} E_p \left(a_M^\dagger(\mathbf{p}, r)a_M(\mathbf{p}, r) - b_M(\mathbf{p}, r)b_M^\dagger(\mathbf{p}, r) \right) + V \frac{m_o^2}{2}\sigma_0^2 \quad (22)$$

From this Hamiltonian, the following Heisenberg equation can be derived:

$$i \begin{pmatrix} \dot{a}_{\mathbf{p}}^{(s)}(t) \\ \dot{b}_{-\mathbf{p}}^{(s)}(t) \end{pmatrix} = \begin{pmatrix} |\mathbf{p}| & M \\ M & -|\mathbf{p}| \end{pmatrix} \begin{pmatrix} a_{\mathbf{p}}^{(s)}(t) \\ b_{-\mathbf{p}}^{(s)}(t) \end{pmatrix} \quad (23)$$

Setting the initial state $a_{\mathbf{p}}^{(s)}(t=0) = a_{M=0}(\mathbf{p}, s)$, the solution reveals that the massive and massless operators are connected via the Bogoliubov transformation:

$$\begin{pmatrix} a_M(\mathbf{p}, r) \\ b_M(\mathbf{p}, r)^\dagger \end{pmatrix} = U(\mathbf{p}, r) \begin{pmatrix} a_0(\mathbf{p}, r) \\ b_0(\mathbf{p}, r)^\dagger \end{pmatrix} U^\dagger(\mathbf{p}, r) \quad (24)$$

where $U(\mathbf{p}, r) = \exp\left\{-\frac{\theta_p}{2}(a_0^\dagger(\mathbf{p}, r)b_0^\dagger(-\mathbf{p}, r) - b_0(-\mathbf{p}, r)a_0(\mathbf{p}, r))\right\}$. The vacuum states for each operator are defined as follows:

$$|\sigma_0\rangle \rightarrow a_M(\mathbf{p}, r)|\sigma_0\rangle = b_M(\mathbf{p}, r)|\sigma_0\rangle = 0 \quad (25)$$

$$|0\rangle \rightarrow a_0(\mathbf{p}, r)|0\rangle = b_0(\mathbf{p}, r)|0\rangle = 0 \quad (26)$$

$a_0(\mathbf{p}, r)^\dagger$ creates an eigenstate of chirality, while $a_M(\mathbf{p}, r)^\dagger$ creates an eigenstate of helicity. Based on the vacuum definition and (24), acting on $|0\rangle$ produces an eigenstate of helicity but not a definite chirality eigenstate. This implies that "chiral symmetry is spontaneously broken".

Thus, the NJL model theoretically predicts vacuum phase transitions. In our universe, it is believed that quark condensation spontaneously breaks chiral symmetry, leading to hadrons acquiring significant masses.

1.4 Quark-Gluon Plasma (QGP)

When hadrons are exposed to extremely high temperatures and densities, they transition into a plasma state known as the Quark-Gluon Plasma (QGP). In the QGP state, quarks are resolved from confinement, and the restoration of chiral symmetry is also expected. Furthermore, it is believed that the universe immediately following the Big Bang was in a QGP state. On the QCD phase diagram, which represents the phase structure of quarks and gluons, the QGP phase appears as shown in Figure 3.

The QGP phase can be observed in high-temperature regions in both high-density and low-density areas. Two types of phase transitions are related in the transition to the QGP phase. The first is the chiral phase transition. The second is the deconfinement-confinement phase transition.

The chiral phase transition is the spontaneous breaking of chiral symmetry as the vacuum undergoes a phase transition, allowing quarks to acquire a substantial effective mass. In other words, the chiral phase transition is deeply related to the mass acquisition of hadrons. The deconfinement-confinement phase transition pertains to the confinement of quarks. In the hadronic ground state, quarks are confined by color interaction. However, in the QGP state, quarks are resolved from confinement and transition into a plasma

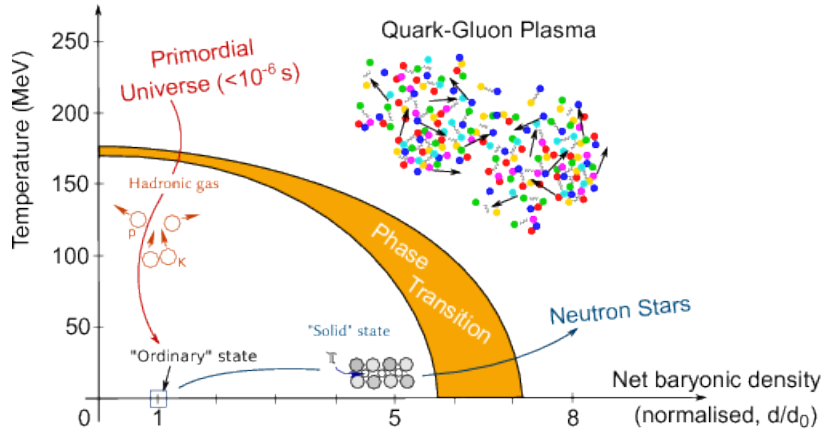


Figure 3: QCD Phase Diagram[3]

state. This is the deconfinement-confinement phase transition. While these transitions are believed to occur at approximately a similar critical temperature, this relationship is not self-evident, and research is still ongoing.

1.5 Heavy Ion collision

The existence of QGP, which are ultrahigh-temperature or dense materials, has been confirmed by heavy-ion collision experiments. As shown in Figure 4, the time evolution proceeds in the following.

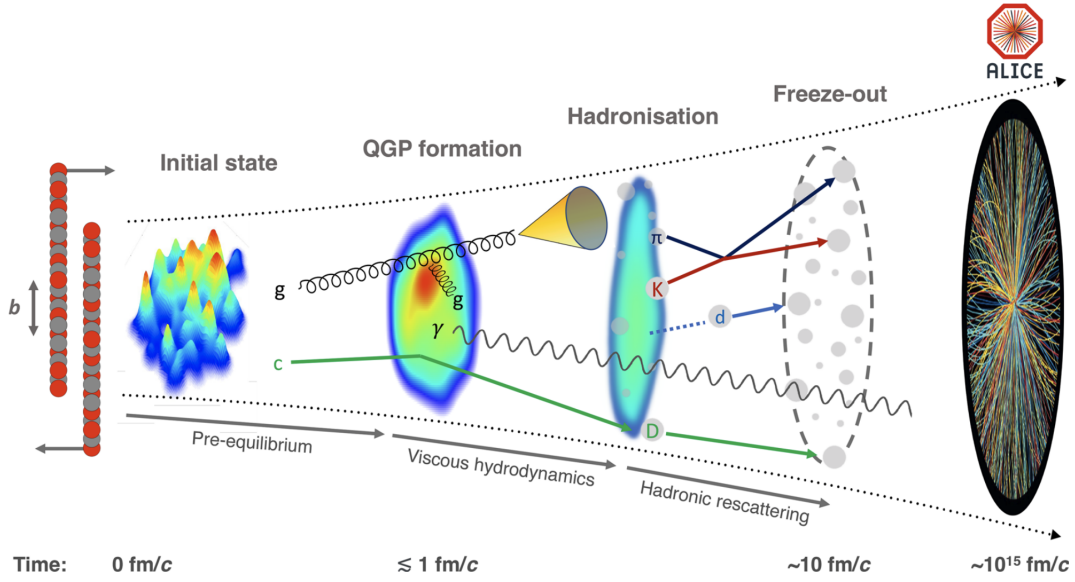


Figure 4: The evolution of a heavy-ion collision at LHC energies[4]

1. Pre-equilibrium state
2. QGP
3. Hadronization

4. Kinetic Freeze-out

In the initial stage of the collision, partons from the nucleons undergo elastic and deep inelastic scatterings to reach thermalization. During this initial collision, phenomena such as jet production and the pair production of heavy quarks occur. Once the material generated in the collision region reaches thermal equilibrium, the system transitions into the QGP state.

In the QGP state, photons and lepton pairs originating from the thermal radiation of high-temperature matter are generated. Jets interact with the QGP and lose energy, resulting in jet quenching, while heavy quarks undergo deconfinement due to the color Debye screening. Subsequently, as the QGP cools, hadronization occurs, leading to chemical freeze-out.

Chemical freeze-out refers to the stop of changes in particle species due to deeply inelastic scatterings among particles. However, elastic scatterings between hadrons continue, and momentum exchange among particles. Later, kinetic freeze-out occurs, fixing the momenta and other properties of the particles. The particles finally detected are those that remain after the kinetic freeze-out. Thus, QGP is formed during the temporal evolution of heavy-ion collisions, and its lifetime is extremely short.

The QGP generated in heavy-ion collisions has its density and temperature determined by the collision energy. High-density QGP regions are realized at collision energies of $\sqrt{s_{NN}} \lesssim 10$ [GeV]. At these energies, the colliding particles stop at the collision point. They create a high-density state where kinetic energy is converted directly into heat, increasing the temperature.

On the other hand, high-temperature, low-density regions are achieved at collision energies of $\sqrt{s_{NN}} \gtrsim 100$ [GeV]. In this energy regime, the colliding particles do not stop but pass through each other, producing a large number of pair creation. As a result, the baryon number density does not become large relative to the temperature. However, a high energy density region leads to the creation of high-temperature matter near the collision point.

In the ALICE experiment, LHC Run 3 operations began in 2022, initiating Pb-Pb collision measurements at $\sqrt{s_{NN}} = 5.36$ TeV. This collision energy produces QGP in the ultrahigh temperature, low-density region. Moreover, compared to the QGP generated at $\sqrt{s_{NN}} = 200$ GeV at RHIC, the higher collision energy at LHC enables the measurement of a larger QGP than ever before.

1.6 Dilepton Measurement[5]

Dilepton measurement is a good probe to investigate the time evolution of heavy-ion collisions. Leptons do not interact with strong interactions, making them less affected by the QGP. This characteristic allows for the measurement of a distribution that sums up

dileptons from all stages of heavy-ion collisions. The sources of dilepton production are as follows:

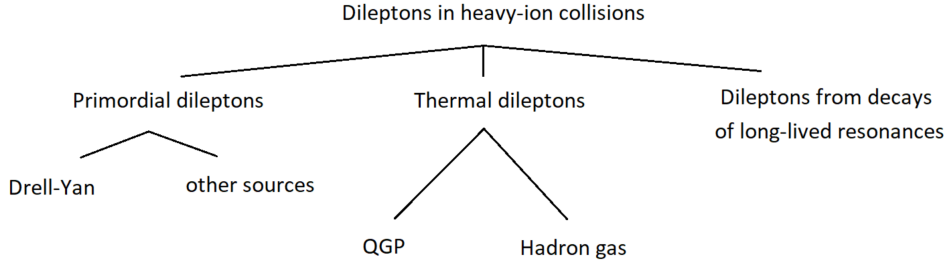


Figure 5: Dilepton source

- Primordial dileptons (from $q\bar{q}$ annihilation)
- Thermal dileptons
- Dileptons from hadron decays

The dilepton mass regions are associated with the time evolution of heavy ion collisions respectively.

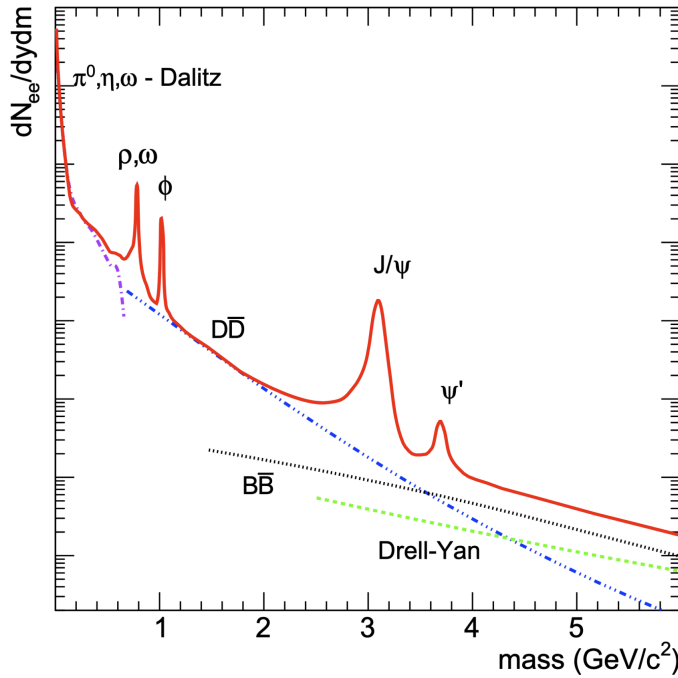


Figure 6: Expected mass spectrum from dileptons[7]

In the High-Mass Region, primordial dileptons (Drell-Yan) constitute the continuum component of the mass distribution. It is related to the initial state of the collision. In the

Intermediate-Mass Region, thermal dileptons originating from the QGP and continuum components such as open-charm and open-beauty are observed.

Finally, in the Low-Mass Region, the dilepton distribution is predominantly derived from light meson decays from the hadronic gas. Most dileptons from hadron decays have longer lifetimes compared to the QGP. So these mesons observed in this region are mostly from the hadron gas. However, light vector mesons (ρ, ω, ϕ) have extremely short lifetimes. They may be affected by QGP.

1.7 Search for chiral symmetry restoration in QGP

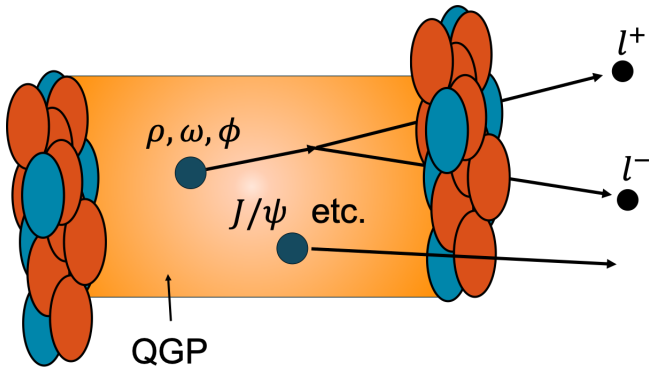


Figure 7: Low mass vector meson decay in QGP

In the QGP, it is expected that an ultra-high temperature and high-density state is realized, leading to $\langle \bar{q}q \rangle \sim 0$ and the restoration of chiral symmetry. Light vector mesons (ρ, ω, ϕ) serve as probes for the masses of hadrons in the QGP. These particles have short lifetimes and decay channels into dileptons. As shown in Fig.4, their short lifetimes make it possible for them to decay within the QGP, which would otherwise immediately hadronize. Additionally, since they decay exclusively into dileptons, which do not undergo strong interactions with the QGP, the masses of hadrons within the QGP can be measured.

In past experiments, the restoration of chiral symmetry was investigated using dileptons. In the SPS-NA60 experiment, the excess of muon pairs in the low-mass region was reported. However, the excess could also be explained by $\pi + \pi \rightarrow \rho \rightarrow \pi\pi$, and thus it did not serve as definitive evidence of chiral symmetry restoration[8].

Additionally, in the electron pair measurements during ALICE Run 2 $\sqrt{s_{NN}} = 5.02$ TeV PbPb collisions, contributions from open-charm and open-beauty were estimated along with the vacuum dilepton distribution excluding ρ , and an excess of electron pairs was reported. The excess was explained as thermal dileptons from the QGP within the error range demonstrated[6].

This study aims to measure the mass modification of light vector mesons in the QGP using forward muon pairs in ALICE Run 3 $\sqrt{s_{NN}} = 5.36$ TeV PbPb collisions. Starting

from ALICE Run 3, the MFT was introduced into the forward detector system of the ALICE experiment. It enables more precise measurements of muon production points compared to Run 2, as well as measurements of muons with lower transverse momentum. By utilizing the differences in muon production points of heavy flavor (HF), which is one of the backgrounds in light vector meson measurements, can be removed. This will allow the precise measurement of the mass distribution of low transverse momentum light vector mesons, which are more likely to decay within the QGP.

1.8 Analysis of pp collision data as a baseline

This paper presents the analysis results of proton-proton collision events. The particles generated in proton-proton collisions are produced from the vacuum. Measurements of collision events where QGP is not produced serve as a baseline for comparison with events where QGP is generated. Currently, the quality of track reconstruction is still insufficient, and the muon pair analysis is also incomplete. Furthermore, the quality of muon tracks in heavy-ion collisions is more challenging than in proton-proton collisions due to the large number of particles generated in each event.

The purpose of this study is to provide an analysis as a baseline for future studies of $\sqrt{s_{NN}} = 5.02$ PbPb collisions, where QGP is expected to be generated and to improve the quality of muon tracks in ALICE Run 3 $\sqrt{s_{NN}} = 13.6$ TeV pp collisions.

2 Detector setup

2.1 Large Hadron Collider (LHC)

The Large Hadron Collider (LHC) is the world's largest circular accelerator. As shown in Figure 8, the LHC and its major experimental groups are located near Geneva, Switzerland. LHC Run 1 was conducted from 2009 to 2013, and Run 2 took place from 2015 to 2018. The ongoing Run 3 is scheduled to collect physics data from 2022 to the summer of 2026. During the run, most of the periods involve proton-proton collision measurements, with heavy-ion collision measurements conducted for about one month each year. The LHC accelerator hosts four major experimental groups: ATLAS, CMS, LHCb, and ALICE.

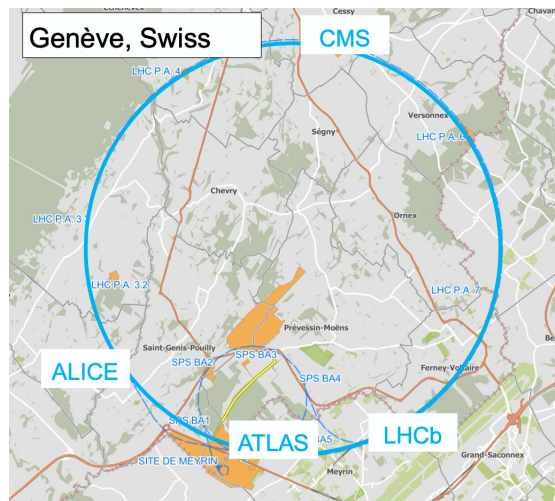


Figure 8: LHC

2.2 A Large Ion Collider Experiment (ALICE)

The ALICE collaboration is an international collaboration consisting of 168 research institutions from 40 countries and around 2,000 researchers. The ALICE detector system is dedicated to research related to the Quark-Gluon Plasma (QGP) produced in heavy-ion collisions. The detectors can be broadly divided into two main groups: the barrel detector group and the forward detector group. The barrel detector group includes detectors such as ITS, TPC, TOF, EMCAL, TRD, PHOS/CPV, and HMPID. A magnetic field is applied along the beam axis, bending the motion of charged particles and enabling particle identification, momentum, and energy measurements. The forward detector group is specifically designed for muon measurements and consists of three trackers—MFT, MCH, and MID—and two hadron absorbers. A dipole magnet is placed between MCH, allowing the measurement of muon momentum and sign. Other detectors include ZDC and FIT. The ZDC is placed far forward from the collision point and measures the number

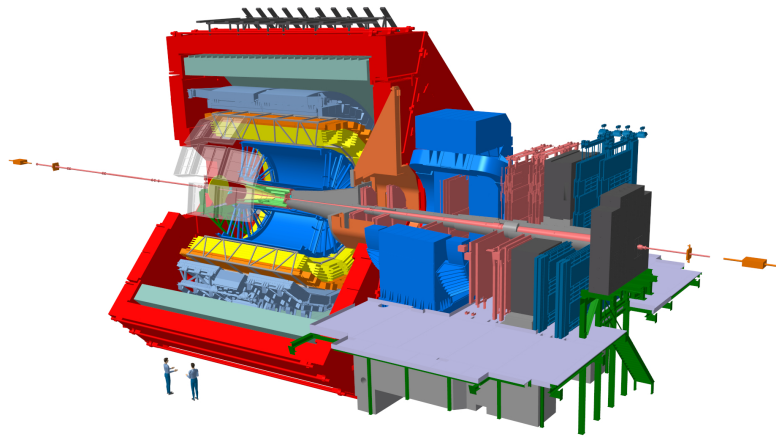


Figure 9: ALICE detectors

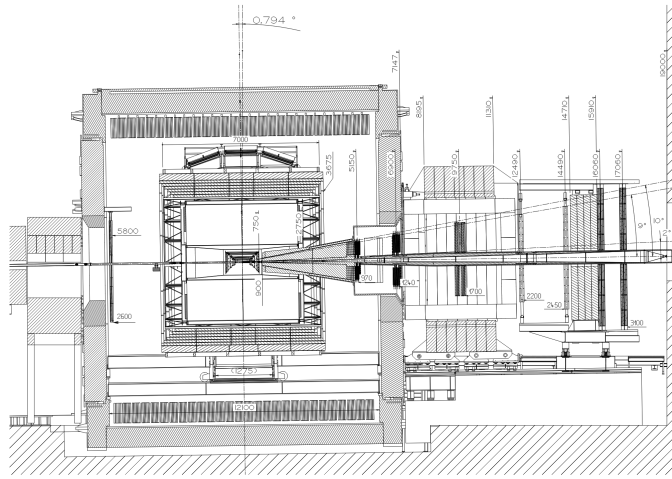


Figure 10: MUON spectrometer

of neutrons and protons, determining the centrality of heavy-ion collision events. The FIT detectors are placed both forward and backward and are used for measuring event luminosity and particle multiplicity.

2.2.1 MUON Spectrometer

The MUON spectrometer consists of the Front Absorber, MCH, Iron Wall, and MID, and has an acceptance range of $-4.0 < \eta < -2.5$. It uses the high penetration power of muons to identify them. Various particles generated at the collision point (IP) pass through the Front Absorber. Hadrons and light electrons, which interact strongly, are absorbed by the Front Absorber. The muons pass through it due to their high penetration power. The muons that pass through the Front Absorber are detected, and any particles such as π mesons that are produced from interactions within the Front Absorber are measured by the MCH. These particles are then absorbed in the Iron Wall, so they are not detected by the MID. Therefore, muon identification (PID) is performed by combining tracks measured

in the MCH and MID. The momentum of the muons is measured using a dipole magnet in the MCH, which is set at a magnetic flux density of 3.0T.

2.2.2 MFT

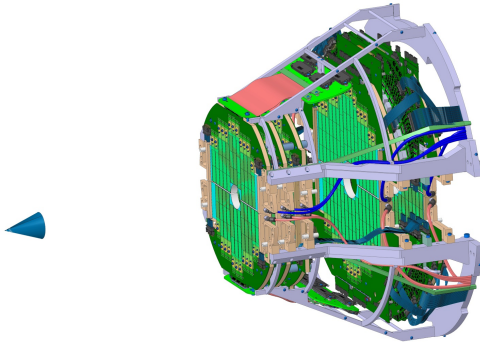


Figure 11: MFT

The MFT is a newly introduced silicon pixel detector in Run 3, installed between $z = 0$ and $z = -76.8$ cm (with an acceptance range of $-3.6 < \eta < -2.5$). It consists of 5 layers of disks that detect tracks and reconstruct MFT standalone tracks considering the influence of the L3 magnet, which creates the ALICE central magnetic field. Since the detector is placed in front of the Front Absorber, the tracks measured include not only muons but also various other particles such as π mesons and kaons. By combining these tracks with those measured by the backward MUON spectrometer, it is possible to measure the DCA of the muons. The ability to measure DCA enables the separation of c and b quarks based on differences in lifetime. Additionally, the precision of the opening angle of the muon pair is improved, which enhances mass resolution. Furthermore, since the MFT is placed in front of the Front Absorber, it allows for the measurement of lower transverse momentum muons compared to those measured by the MUON spectrometer alone.

2.2.3 MFT-MUON Track Matching

The tracks measured by the MUON spectrometer and MFT are matched to reconstruct the Global Track. First, the tracks measured by the MUON spectrometer are extrapolated toward the collision point up to the last disk of the MFT, located at $z = 76.8$ cm. The extrapolation accounts for multiple scattering and energy loss corrections in the hadron absorber between the MUON spectrometer and MFT. Then, suitable MFT tracks are selected based on both position and direction, and the matching quality is evaluated by comparing the position and slope of the tracks. The best quality MFT track is selected and used to construct the Global Track.

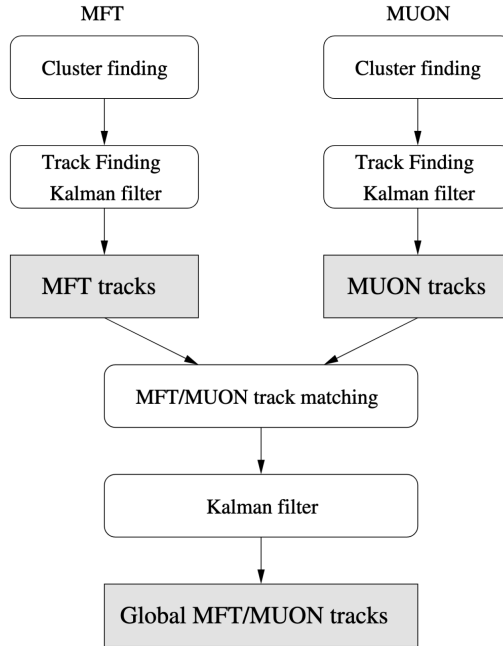


Figure 12: Global Track[9]

3 Analysis

3.1 DataSet

The data used is a part of pp collisions at $\sqrt{s} = 13.6$ TeV obtained in 2022. The collision rate of pp is 500 kHz, and the dataset name is LHC22o_apass7. The Monte Carlo simulation data used in 3.7 utilized Pythia8 Monash to reproduce 500 kHz pp collisions at $\sqrt{s} = 13.6$ TeV, employing minimum bias event simulations without extracting specific events.

3.2 Event selection

The position of the proton-proton collision was measured by the ITS detector system. The Z-coordinate of the collision point, denoted as $VtxZ$, was selected with the condition $|VtxZ| < 10$ cm, using the ITS center at $Z = 0$ as the reference. This cut value is aligned with the ITS acceptance. The number of events obtained with this cut is 5.5×10^9 .

3.3 Single muon track reconstruction

As described in 2.2.3, the reconstructed Global Track was used to calculate various physical quantities of the muon as follows: The muon's η and ϕ were calculated using the MFT standalone Track. The momentum p was derived by propagating the MCH standalone track to the Z-coordinate of the collision point, with corrections applied for multiple scat-

tering and energy loss in the absorber. For the DCA, a Global Fit was performed for all tracks constituting the Global Track, and the resulting track was used. As shown in Fig. 13, the track was linearly extrapolated to the Z-coordinate of the collision point (IP), and the distance between the extrapolated point and the collision point was calculated as the DCA. Similarly, using the same track, R_{abs} was calculated as the distance from the beam axis at the back edge of the absorber, as shown in Fig. 14. Furthermore, the MFT-MCH matching χ^2 was calculated based on the parameter differences when extrapolating the MFT track and MCH track to the matching plane.

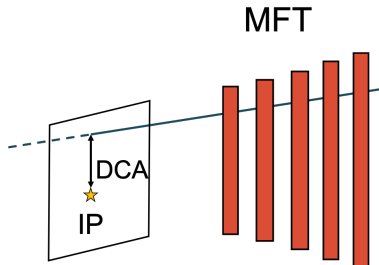


Figure 13: conceptual scheme of DCA

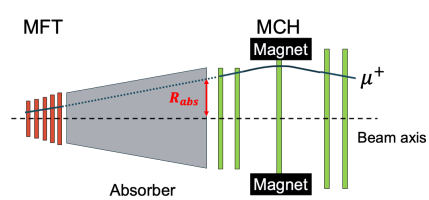


Figure 14: conceptual scheme of R_{abs}

3.4 Single muon selection

The cuts applied to the obtained muon tracks are as follows:

- $-3.6 < \eta < -2.5$
- $17.5 \text{ cm} < R_{abs} < 89.5 \text{ cm}$
- $pDCA < 6\sigma$
- MFT-MCH matching $\chi^2 < 30$

The η cut is aligned with the MFT-MHC-MID acceptance. The R_{abs} cut value is set to exclude values that are influenced by the presence of the hadron absorber rear end. The $pDCA$ is the product of momentum and DCA , and this cut is applied to remove muons originating from beam gas. Tracks with $pDCA$ larger than 6σ when fitted with a Gaussian distribution are excluded. The final MFT-MCH matching χ^2 value is obtained from a fit using the detected points of the MFT and MCH tracks when matching them. The value used in this study is optimized, as described later, to maximize the statistical uncertainty of the yields for ω and ϕ .

3.5 Dimuon analysis

3.5.1 Dimuon reconstruction

Using the single muons selected in 3.4, dimuons are reconstructed. The mass($M_{\mu\mu}$), transverse momentum(p_T), pseudorapidity(η), and Azimuth angle(ϕ) of the dimuon are

calculated as (28) (34). First, the p_T , η , and ϕ of the single muons are converted into four-component vectors (p_x, p_y, p_z, E) using (28),(29),(30),(30).

$$p_x = p_T \cos(\phi) \quad (27)$$

$$p_y = p_T \sin(\phi) \quad (28)$$

$$p_z = p_T \sinh(\eta) \quad (29)$$

$$E = \sqrt{p_T^2 \cosh^2(\eta) + m_\mu^2} \quad (30)$$

Then, using the (p_x, p_y, p_z, E) of the single muons, the $(P_x, P_y, P_z, E_{\mu\mu})$ of the dimuon are calculated.

$$\begin{pmatrix} P_x \\ P_y \\ P_z \\ E \end{pmatrix} = \begin{pmatrix} p_{x1} \\ p_{y1} \\ p_{z1} \\ E_1 \end{pmatrix} + \begin{pmatrix} p_{x2} \\ p_{y2} \\ p_{z2} \\ E_2 \end{pmatrix} \quad (31)$$

Using the obtained four-component vector of the dimuon $(P_x, P_y, P_z, E_{\mu\mu})$, the pair's $M_{\mu\mu}$, p_T , and η were calculated from the (33),(34),(34).

$$M_{\mu\mu} = \sqrt{E^2 - (p_x^2 + p_y^2 + p_z^2)} \quad (32)$$

$$p_{T\mu\mu} = \sqrt{p_x^2 + p_y^2} \quad (33)$$

$$\eta_{\mu\mu} = -\log \left(\tan \left(\frac{1}{2} \arctan \left(\frac{\sqrt{p_x^2 + p_y^2}}{p_z} \right) \right) \right) \quad (34)$$

Using the above formulas, the physical quantities of the dimuon are calculated.

3.5.2 Combinatorial background subtraction

Muons detected by the detector cannot be distinguished from which parent particle they originated. Therefore, when forming the muon pairs, all the μ^+ and μ^- are paired within each collision event, and the mass is reconstructed. Then, the uncorrelated mass distribution is estimated and subtracted later. By doing so, the mass distribution of the correlated muon pairs can be obtained. In this study, the Like-sign method was used. The Like-sign method estimates the uncorrelated background events using the mass distribution of same-sign muon pairs obtained from the same event. The formula is as follows:

$$\frac{dN_{sig}}{dm} = \frac{dN_{same}^{+-}}{dm} - 2R \sqrt{\frac{dN_{same}^{++}}{dm} \frac{dN_{same}^{--}}{dm}} \quad (35)$$

$$2R = \frac{\frac{dN_{mix}^{+-}}{dm}}{\sqrt{\frac{dN_{mix}^{++}}{dm} \frac{dN_{mix}^{--}}{dm}}} \quad (36)$$

where, $\frac{dN_{sig}}{dm}$ represents the number of correlated muons at each mass, $\frac{dN_{same}^{**}}{dm}$ represents the number of same-sign muon pairs in the same event (** corresponds to the muon sign),

and $\frac{dN_{mix}^{**}}{dm}$ represents the number of muon pairs formed from different events. R is a term to correct for the acceptance difference due to the muon sign. If there is no acceptance difference due to the sign, R = 1. In this analysis, since muon pairs from different events were not combined, R = 1 was used for the calculation. The characteristic of the Like-sign method is that it subtracts uncorrelated background events using same-sign muon pairs from the same event. This allows for the subtraction of weakly correlated particles within each event, such as those caused by elliptic flow in heavy-ion collisions. The uncorrelated background events estimated by the Like-sign method depend on the p_T of the dimuon. Therefore, the mass distributions were separated by the p_T of the dimuon, and for each invariant mass distribution, the uncorrelated background events were subtracted using the Like-sign method. The resulting subtracted plots are shown in Figures ?? to ??.

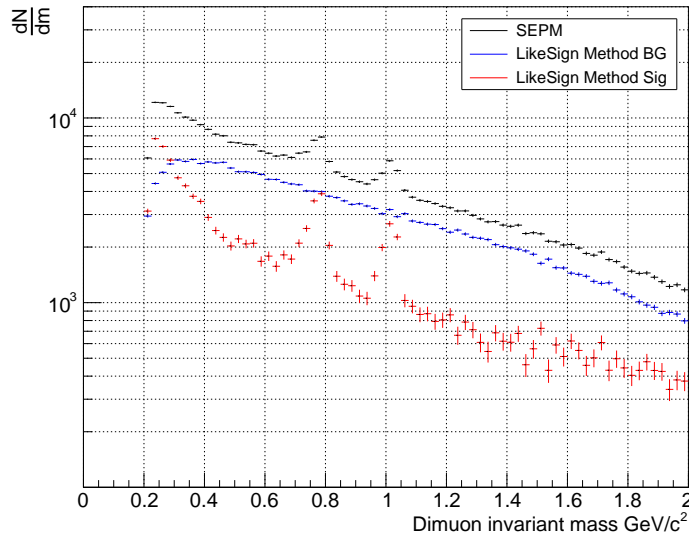


Figure 15: $1 < p_T < 30$

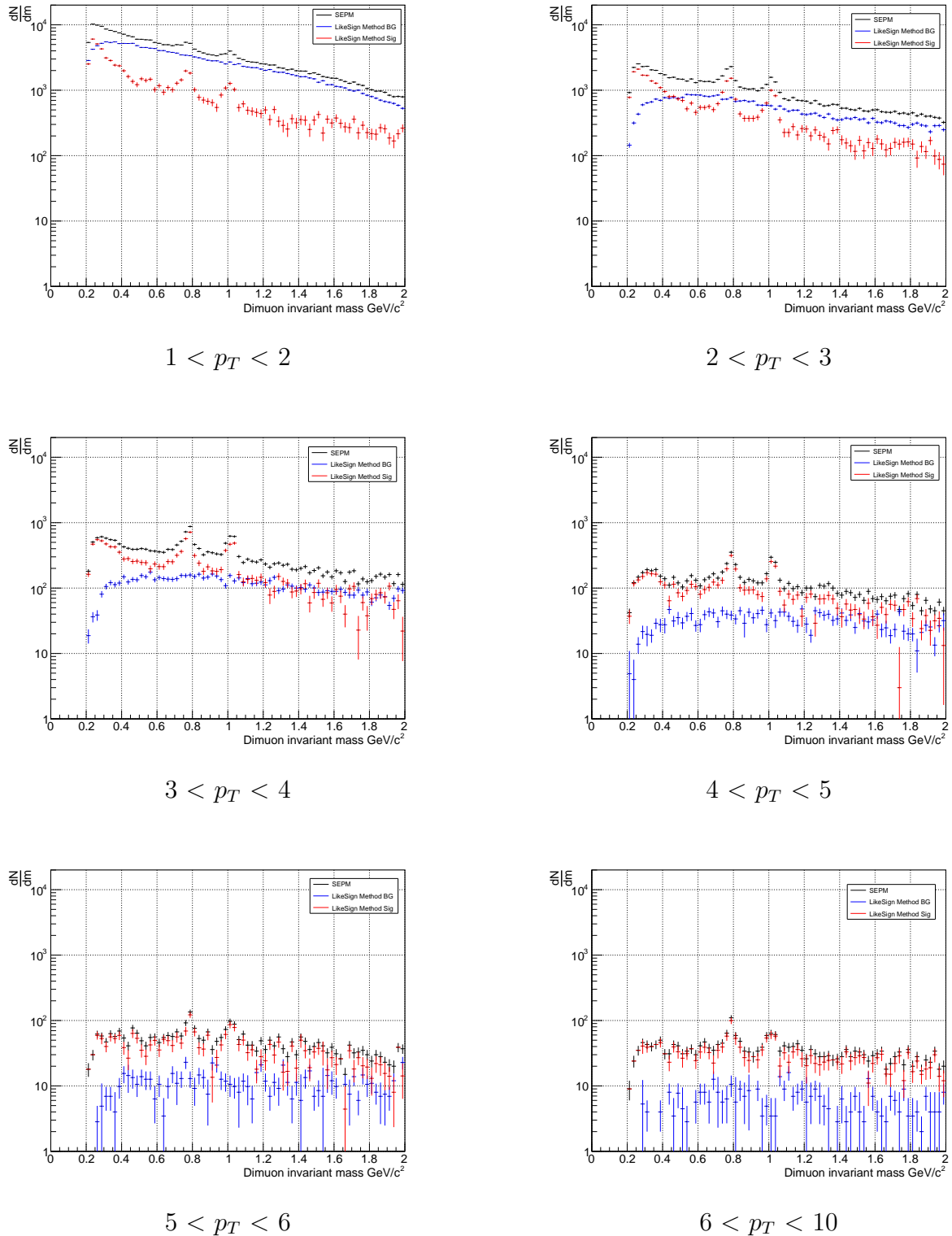


Figure 16: Result of combinatorial background subtraction of each p_T

The black line represents the distribution obtained by pairing muons with opposite charges within the same event and reconstructing the mass. The blue line represents the estimated uncorrelated background events using the Like-sign method. The red line represents the distribution obtained by subtracting the blue distribution from the black

distribution, which corresponds to the correlated dimuon invariant mass distribution. In the $0 < p_T < 1(\text{GeV})$ region, the MFT-MCH matching quality was insufficient, and no peaks for ω and ϕ were observed. The $6 < p_T < 10(\text{GeV})$ region was taken wider than other transverse momentum regions to preserve the statistical significance.

3.5.3 Peak extraction of $\omega \rightarrow \mu\mu, \phi \rightarrow \mu\mu$

The distributions of the correlated dimuon invariant mass obtained from 3.5.2 are used to extract the distributions of $\omega \rightarrow \mu\mu, \phi \rightarrow \mu\mu$. The dimuon invariant mass distribution under 2(GeV) contains pairs of muons coming from light mesons and open HF:

- $\eta \rightarrow \mu^+ \mu^-$
- $\eta \rightarrow \mu^+ \mu^- \gamma$
- $\rho \rightarrow \mu^+ \mu^-$
- $\omega \rightarrow \mu^+ \mu^-$
- $\omega \rightarrow \mu^+ \mu^- \pi^0$
- $\eta' \rightarrow \mu^+ \mu^- \gamma$
- $\phi \rightarrow \mu^+ \mu^-$
- $c\bar{c} \rightarrow D\bar{D} \rightarrow \mu^+ \mu^- + \text{others}$
- $b\bar{b} \rightarrow B\bar{B} \rightarrow \mu^+ \mu^- + \text{others}$

The $\omega \rightarrow \mu\mu, \phi \rightarrow \mu\mu$ processes each have sharp peak structures with peaks around 0.8GeV and 1.0GeV in the mass distribution. In this analysis, all distributions other than these are considered background events. Therefore, an exponential fit is performed to the continuous component of the mass distribution, and only the peaks are extracted. The fit function is as follows:

$$f(m) = N_0 * \exp\{-p1 * m\} + N_\omega * \exp\left\{-\frac{1}{2}\left(\frac{m - M_\omega}{\sigma_\omega}\right)^2\right\} + N_\phi * \exp\left\{-\frac{1}{2}\left(\frac{m - M_\phi}{\sigma_\phi}\right)^2\right\} \quad (37)$$

where, $N_0, N_\omega, N_\phi, M_\omega, M_\phi, \sigma_\omega, \sigma_\phi$ are fit parameters, with M_ω and M_ϕ representing the mean mass positions of ω and ϕ , and σ_ω and σ_ϕ corresponding to the mass widths. This fit function was applied to the correlated invariant mass distributions in ?? ???. The results are shown in ?? ??.

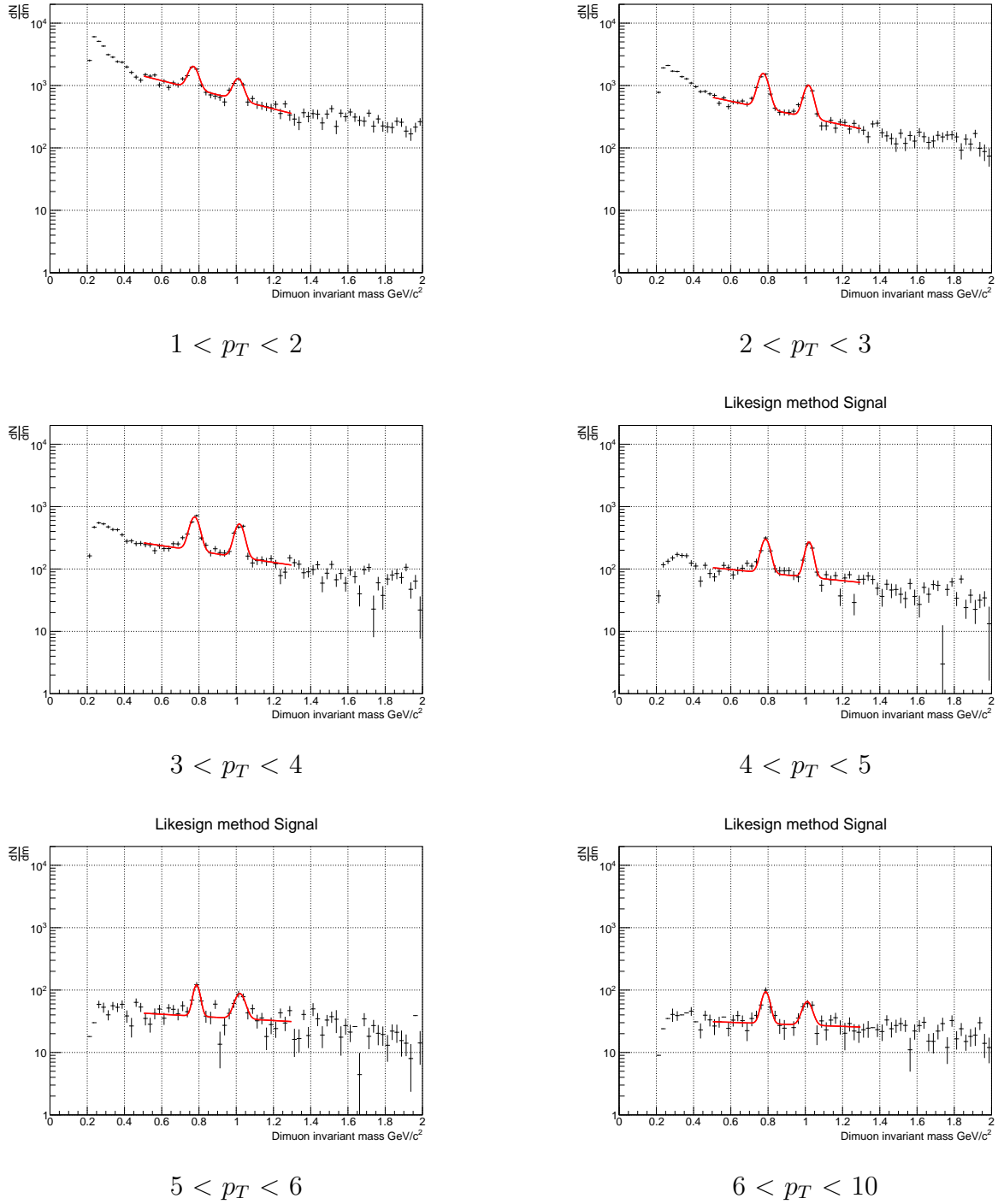


Figure 17: fit result of each pt

The mean mass positions and mass widths for ω and ϕ , as well as the fit χ^2 values for each transverse momentum region, are summarized in the following table.

3.5.4 Yield calculation of ω, ϕ

Using the mean mass position and mass width of $\omega \rightarrow \mu\mu$ and $\phi \rightarrow \mu\mu$ obtained from the above fit, the yield for each meson was calculated. The number of dimuons falling within

Table 1: Fit Results

	ω mean mass	ω mass width	ϕ mean mass	ϕ mass width	fit χ^2
$1 < p_T < 2$	0.769 ± 0.002	0.026 ± 0.002	1.01 ± 0.00	0.026 ± 0.003	34.71/24
$2 < p_T < 3$	0.774 ± 0.001	0.026 ± 0.001	1.016 ± 0.002	0.024 ± 0.001	44.32/24
$3 < p_T < 4$	0.776 ± 0.002	0.025 ± 0.002	1.017 ± 0.002	0.025 ± 0.001	71.93/24
$4 < p_T < 5$	0.787 ± 0.002	0.023 ± 0.002	1.02 ± 0.00	0.021 ± 0.002	45.63/24
$5 < p_T < 6$	0.787 ± 0.003	0.018 ± 0.003	1.02 ± 0.005	0.027 ± 0.006	41.72/24
$6 < p_T < 10$	0.787 ± 0.004	0.021 ± 0.005	1.01 ± 0.01	0.025 ± 0.004	16.18/22

3σ of each Gaussian was calculated as the yield for ω and ϕ , respectively.

$$\min = -3 \times \sigma + M \quad (38)$$

$$\max = 3 \times \sigma + M \quad (39)$$

$$\text{Yield} = \sum_{\text{min}}^{\text{max}} F(m) \quad (40)$$

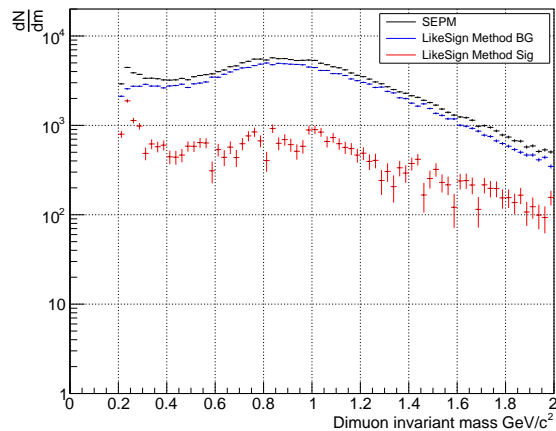
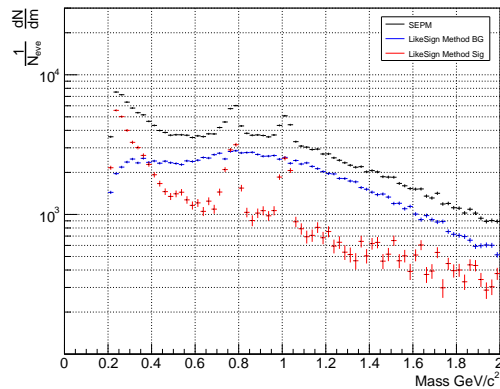
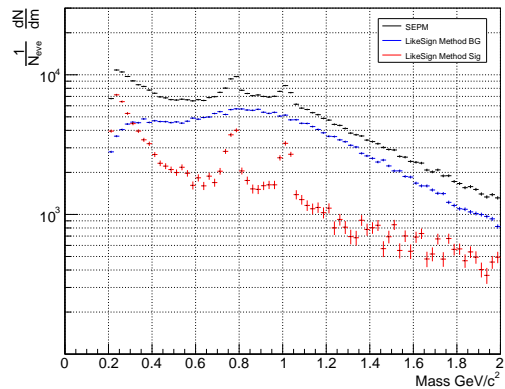
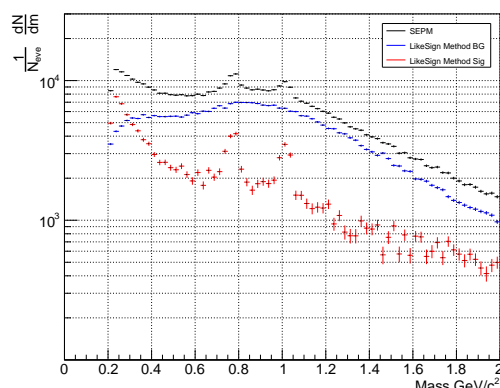
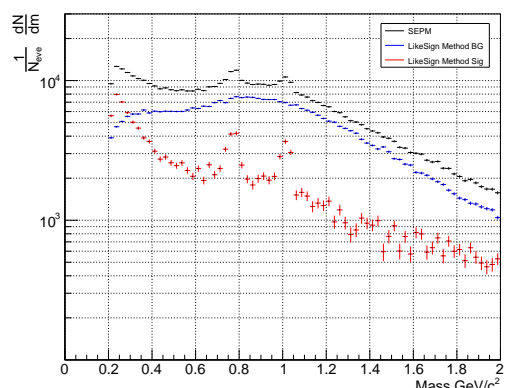
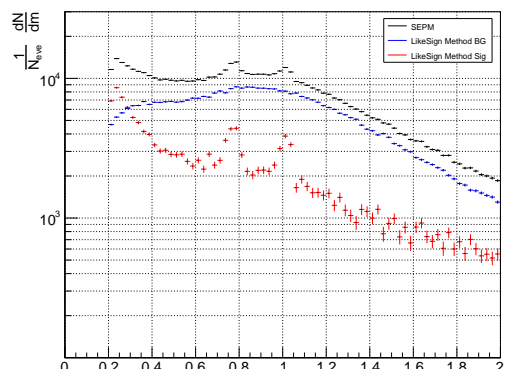
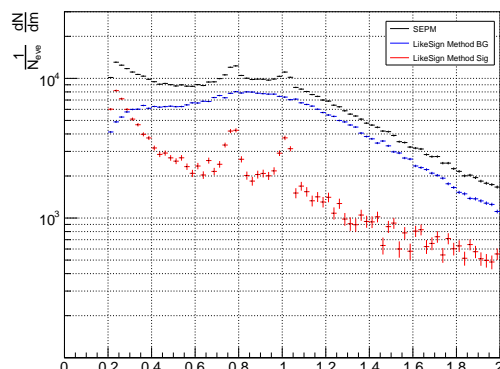
Table 2: Fit Results

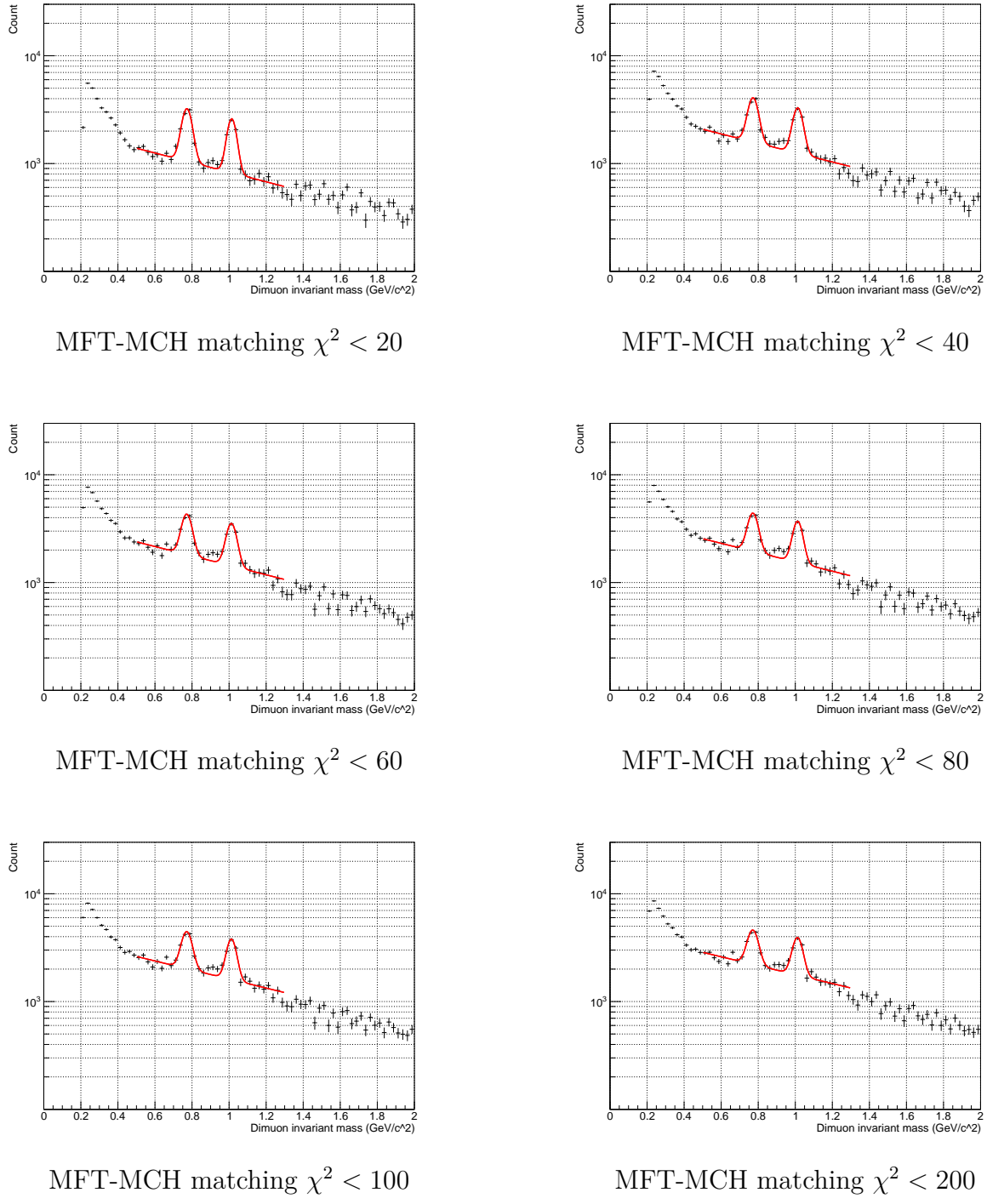
	ω Yield	ϕ Yield
$1 < p_T < 2$	$(3.00 \pm 0.24) \times 10^3$	$(1.83 \pm 0.21) \times 10^3$
$2 < p_T < 3$	$(3.11 \pm 0.14) \times 10^3$	$(1.75 \pm 0.11) \times 10^3$
$3 < p_T < 4$	$(1.331 \pm 0.070) \times 10^3$	$(0.902 \pm 0.062) \times 10^3$
$4 < p_T < 5$	$(0.538 \pm 0.042) \times 10^3$	$(0.387 \pm 0.037) \times 10^3$
$5 < p_T < 6$	$(0.150 \pm 0.022) \times 10^3$	$(0.144 \pm 0.024) \times 10^3$
$6 < p_T < 10$	$(0.037 \pm 0.0057) \times 10^3$	$(0.023 \pm 0.050) \times 10^3$

3.6 Analysis for improving MFT-MCH matching purity

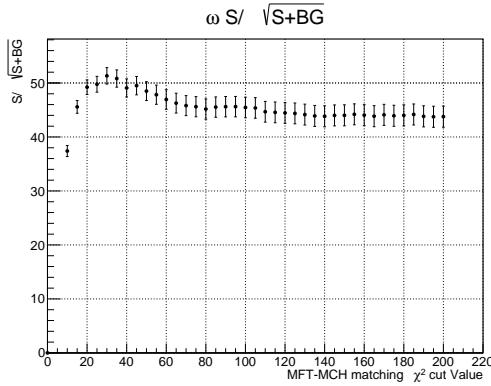
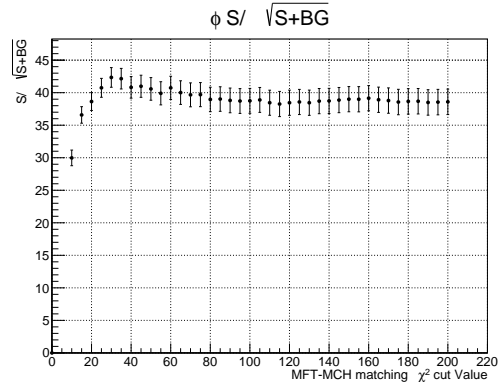
3.6.1 MFT-MCH matching χ^2 Optimization

Using the yield analysis method for $\omega \rightarrow \mu\mu$ and $\phi \rightarrow \mu\mu$ as in 3.5.2, the optimization of the MFT-MCH matching χ^2 for the Single muon Track was performed. The MFT-MCH matching χ^2 is the χ^2 value obtained when matching the tracks from MFT and MCH, and large values are considered indicative of fake matches. This value was optimized such that the statistical error of each yield is minimized. First, the mass distribution was constructed using only muon tracks with an MFT-MCH matching $\chi^2 <$ value, and a fit was performed as described above. The results are shown in the figures below.

Figure 18: Combinatorial subtraction of dimuon $0 < p_T < 1$ MFT-MCH matching $\chi^2 < 20$ MFT-MCH matching $\chi^2 < 40$ MFT-MCH matching $\chi^2 < 60$ MFT-MCH matching $\chi^2 < 80$ 

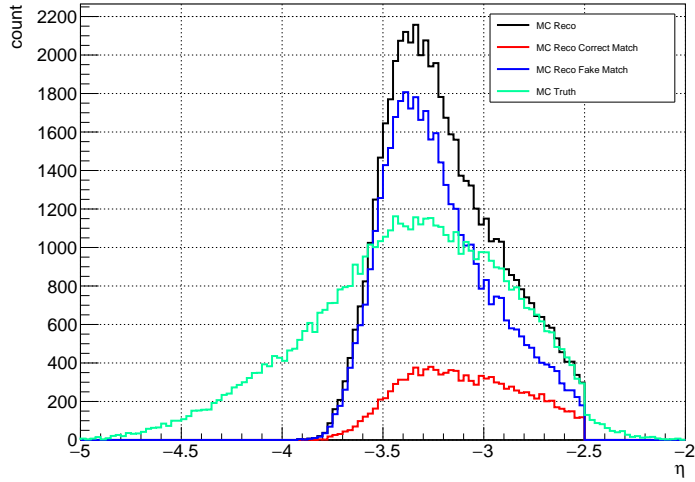
Figure 20: MFT-MCH matching χ^2

Similarly, from the fit results, the yields for $\omega \rightarrow \mu\mu$ and $\phi \rightarrow \mu\mu$ were obtained. These yields were then normalized by dividing by the number of dimuons in the same mass region, and the optimization was performed to maximize $S/\sqrt{S + BG}$. The resulting plot is shown below, where the x-axis is the matching χ^2 and the y-axis is $S/\sqrt{S + BG}$. From this, it is observed that the optimal value for the matching χ^2 is $\chi^2 < 30$.

Figure 21: ω figure of meritFigure 22: ϕ figure of merit

3.7 Fake Match Track Removal Analysis of MFT-MCH-MID Track using MFT Track η - MCH Track η

The matching of MFT Tracks located before the hadron absorption pair and MCH Tracks located behind them is important for the quality of physical quantities such as single muon p_T and η . Here, we performed an analysis to remove MFT-MCH-MID tracks, which match incorrect tracks, by applying cuts to the already reconstructed Global Tracks using three detectors. The dataset used is LHC24b1, which is a Monte Carlo dataset for $pp\sqrt{s} = 13.6\text{TeV}$ minimum-bias events. This simulation data is detailed in

Figure 23: η distribution of Global Track

The tracks reconstructed with MFT-MCH-MID tracks, as shown in 23, include tracks reconstructed outside the acceptance. The black histogram shows the η distribution of the reconstructed Global Tracks. Blue represents the η distribution of fake match tracks, and red represents the η distribution of correct match tracks. The green distribution

corresponds to the true η distribution for the black tracks. By comparing the green and black distributions, we observe that muons outside the acceptance are reconstructed, and they form the distribution of fake matches. To remove such tracks, we applied the following $\Delta\eta$ cut:

$$\Delta\eta = \text{MFT } \eta - \text{MCH } \eta \quad (41)$$

We calculated $\Delta\eta$ for each track and examined the distributions of fake match tracks and correct match tracks. The resulting distributions are shown in the following figure, where blue represents the fake match distribution and red represents the correct match distribution.

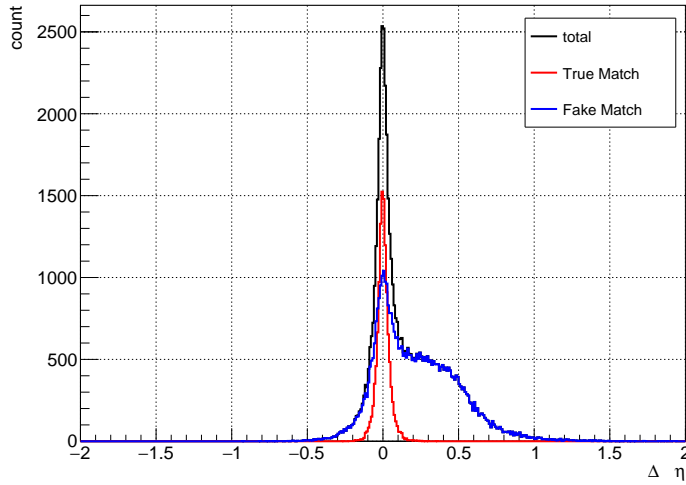


Figure 24: $\Delta\eta$ distribution

From 24, we see that for $\Delta\eta > 0.2$, fake match tracks dominate. To remove fake matches while preserving as many correct matches as possible, we applied a $\Delta\eta < 0.2$ cut. The distributions of each physical quantity after this cut are as follows.

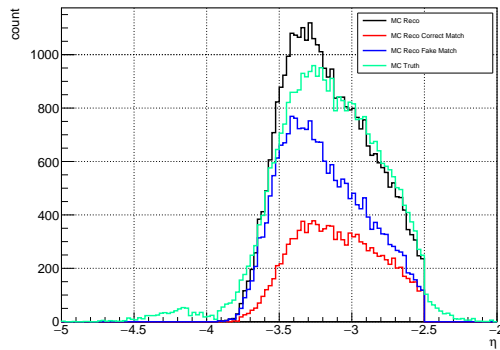


Figure 25: The η distribution of Global Tracks after the $\Delta\eta$ cut

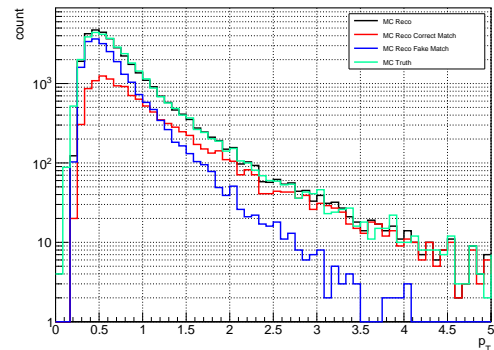
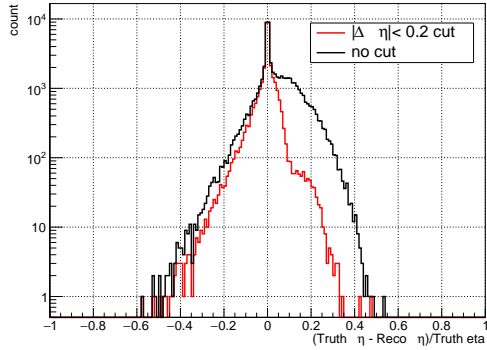
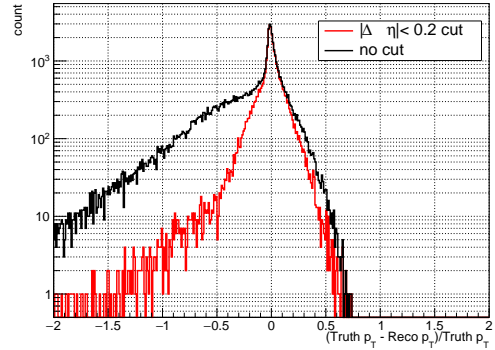
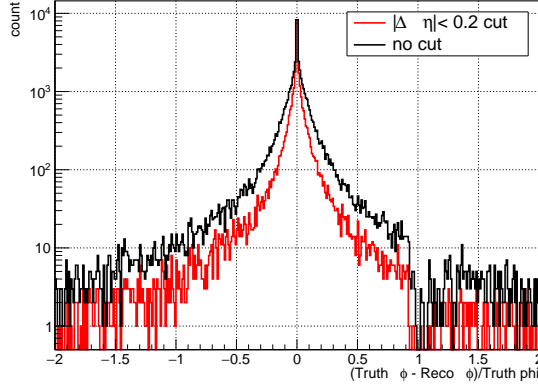


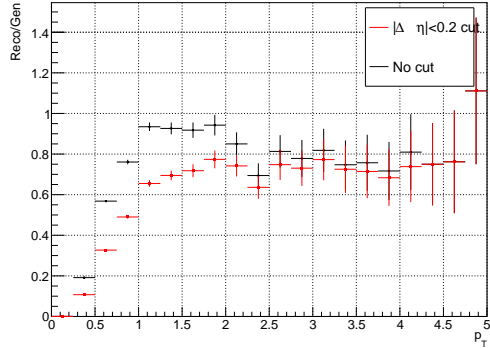
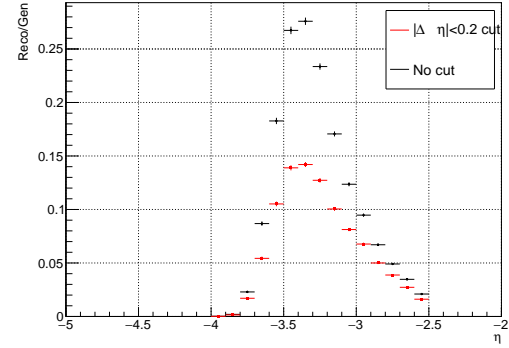
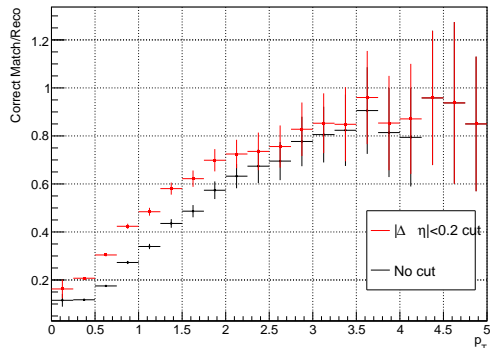
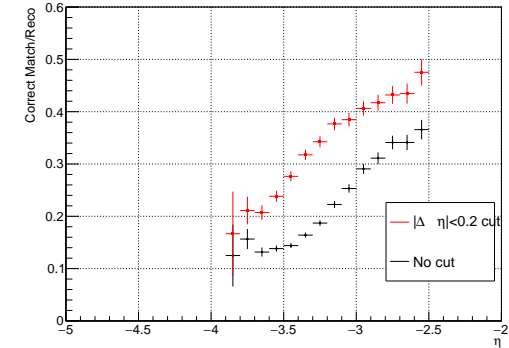
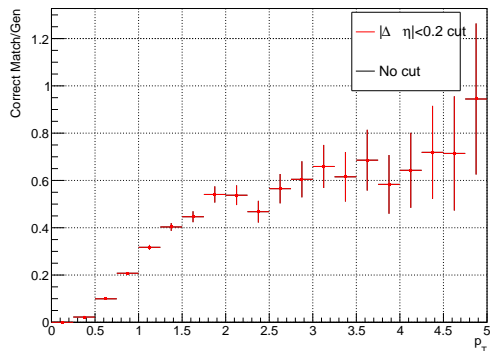
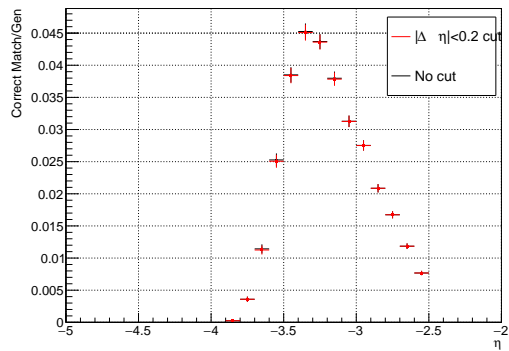
Figure 26: The p_T distribution of Global Tracks after the $\Delta\eta$ cut

In ??, all reconstructed tracks are shown in black, with red representing correct match tracks, and green representing the true muon track distribution. By comparing the green distribution in ??, we observe that after the cut, tracks outside the acceptance have been removed. However, fake match tracks inside the acceptance remain. As shown in the p_T distribution, there are still many fake match tracks at low p_T . The resolution of each physical quantity is shown below.

Figure 27: Resolution of η Figure 28: Resolution of p_T Figure 29: Resolution of ϕ

The horizontal axis shows the difference between the reconstructed values and the true values, divided by the true values, while the vertical axis represents the number of occurrences. The black histogram represents the resolution without applying the $\Delta\eta$ cut, and the red histogram represents the tracks after applying the $\Delta\eta < 0.2$ cut. By comparing the black and red histograms, we can see that all distributions show improved resolution for single muons. Furthermore, efficiency and matching purity are provided below.

The chosen cut value ($\Delta\eta < 0.2$) was selected to discard only the fake match tracks while keeping the correct match tracks, so the efficiency is reduced, but the matching purity has improved. The efficiency \times purity value remains almost unchanged before and after the cut.

Efficency of p_T Efficency of η Figure 32: Purity of p_T Figure 33: Purity of η Figure 34: Efficency \times Purity of p_T Figure 35: Efficency \times Purity of η

4 Results and Outlook

This is the p_T spectrum of the yield for ω and ϕ . Since the cross section has not been calculated for the vertical axis yet, a comparison with other experimental results cannot be made. However, a distribution with an exponential dependence on p_T can be observed. As for future prospects, simulations of $\omega \rightarrow \mu\mu$ and $\phi \rightarrow \mu\mu$ will be conducted, followed by

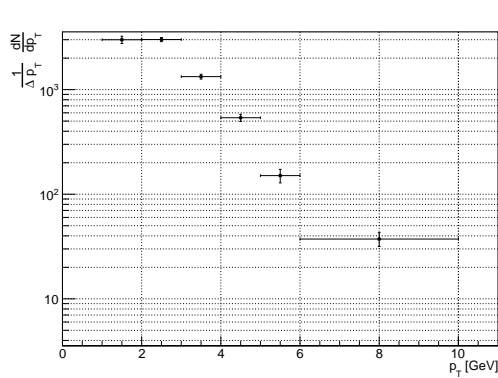


Figure 36: ω yield

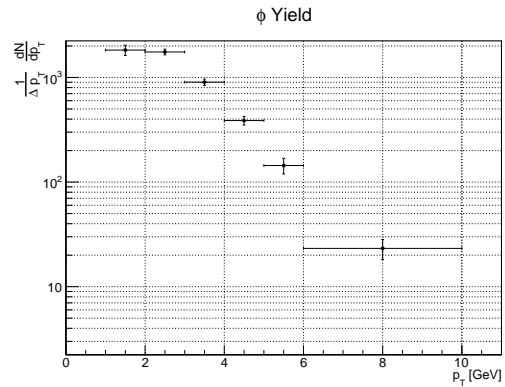


Figure 37: ϕ yield

acceptance \times efficiency corrections. The goal is to determine the production cross-section for ω and ϕ in forward muon pairs.

5 Acknowledgements

References

- [1] S. Navas *et al.* [Particle Data Group], Phys. Rev. D **110**, no.3, 030001 (2024) doi:10.1103/PhysRevD.110.030001
- [2] W. Weise, Nucl. Phys. A **553**, 59C-72C (1993) doi:10.1016/0375-9474(93)90615-5
- [3] A. Maire, "Phase diagram of QCD matter: Quark-Gluon Plasma," 2015. Available at: <https://cds.cern.ch/record/2025215>
- [4] ALICE Collaboration., Acharya, S., Adamová, D. et al. The ALICE experiment: a journey through QCD. Eur. Phys. J. C **84**, 813 (2024). <https://doi.org/10.1140/epjc/s10052-024-12935-y>
- [5] F. Geurts and R. A. Tripolt, Prog. Part. Nucl. Phys. **128**, 104004 (2023) doi:10.1016/j.ppnp.2022.104004 [arXiv:2210.01622 [hep-ph]].
- [6] S. Acharya *et al.* [ALICE], [arXiv:2308.16704 [nucl-ex]].
- [7] R. Rapp and J. Wambach, Adv. Nucl. Phys. **25**, 1 (2000) doi:10.1007/0-306-47101-9_1 [arXiv:hep-ph/9909229 [hep-ph]].
- [8] S. Damjanovic *et al.* [NA60], Nucl. Phys. A **783**, 327-334 (2007) doi:10.1016/j.nuclphysa.2006.11.015 [arXiv:nucl-ex/0701015 [nucl-ex]].
- [9] "Technical Design Report for the Muon Forward Tracker," CERN-LHCC-2015-001, ALICE-TDR-018, 2015. Available at